Journal of Materials Chemistry C

ROYAL SOCIETY OF CHEMISTRY

COMMUNICATION

View Article Online
View Journal | View Issue

Check for updates

Cite this: J. Mater. Chem. C, 2022, 10, 13762

Received 18th March 2022,
Accepted 12th July 2022

DOI: 10.1039/d2tc01109c

rsc.li/materials-c

Published on 14 suoidnemánnu 2022. Downloaded on 2026-06-02 13:51:14.

Multi-material 3D printing-enabled multilayers for smart actuation *via* magnetic and thermal stimuli†

Dharneedar Ravichandran,[a] Reza James Ahmed,[b] Rounak Banerjee,[c] Mahdi Ilami,[b] Hamid Marvi,[d] Guillaume Miquelard-Garnier,[e] Yuval Golan[f] and Kenan Song*[g]

Transitional compositions or phase-changing structures in specific layers can respond to environmental changes differently and show intelligent behaviors. For example, smart polymers with shape morphing capabilities (*e.g.*, external field-controlled untethered actuation) have found applications in angle-changing solar panel support, crawling soft microrobots, targeted drug delivery, tissue scaffolds, and directional heat dissipation in microelectronics. However, conventional processing has constraints in layer stacking, thus limiting the manufacturing efficiency, structural flexibility, and material compatibility. Therefore, this research will leverage an in-house 3D printing platform for rapidly prototyped, multi-material, and multiphase layers. Furthermore, our multiphase direct ink writing (MDIW) 3D printing allows for a one-step assembly of different polymers and nanoparticles in composite multilayers within each printed line (*e.g.*, a microscale resolution). To demonstrate the smart actuation *via* thermal and magnetic fields, we selected ester- and ether-based thermoplastic polyurethane (TPU) polymers, polycaprolactone (PCL), and iron oxide (Fe_3O_4) nanoparticles that are selectively mixed and combined as printing feedstocks. The particular position of different polymers and particles led to layers with distinct anisotropy, enabling varying actuation efficiency when these composites were fixed at different orientations with respect to the printing texture. As a result of the unique 3D printing platform and composite microstructures, this research provides an efficient protocol for fabricating multiphase composite layers with smart behaviors for broad applications.

Introduction

Small scale soft robots from millimeter to micrometer size have gained immense interest because of their ability to morph and access unreachable and confined locations.[1] These robots, possessing a small footprint yet flexible load-carrying ability to reach tiny spaces, have found wide applications as drug carriers, minimally invasive surgeries, field explorations, medical implants, and space missions.[2,3] However, many soft robots operated through wired connections with circuit control

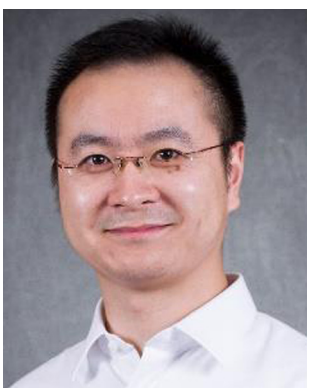

Kenan Song

Kenan Song is currently an assistant professor at Arizona State University (ASU). He obtained his PhD. in Mechanical Engineering from Northeastern University (2015) and trained as a Postdoc in Chemical Engineering and Materials Science and Engineering departments at MIT (2015–2017) before joining ASU. Dr Song's current research includes textile engineering, coating technology, and 3D printing, especially the innovative use of manufacturing tools in tuning material dimensions (e.g., 1D fibers, 2D coatings, and 3D layers), types (e.g., polymers, nanoparticles), mesoscale structures (e.g., polymer chemistry, nanoparticle morphologies, composite interfaces), and properties (e.g., mechanical, thermal, electrical, optical, and stimuli responsive behaviors).

[a] Systems Engineering, School of Manufacturing Systems and Networks, The Polytechnic School (TPS), Ira A. Fulton Schools of Engineering, Arizona State University, Mesa, AZ, 85212, USA
[b] Mechanical Engineering, The School of Engineering of Matter, Transport and Energy (SEMTE), Ira A. Fulton Schools of Engineering, Arizona State University, Tempe, AZ, 85281, USA
[c] Department of Physics, The College of Liberal Arts and Science, Arizona State University, Tempe, AZ, 85281, USA
[d] The School of Engineering of Matter, Transport and Energy (SEMTE), Ira A. Fulton Schools of Engineering, Arizona State University, Mesa, AZ, 85281, USA
[e] Laboratoire PIMM, UMR 8006, Arts et Métiers Institute of Technology, CNRS, CNAM, Hesam University, 151 boulevard de L'Hôpital, 75013, Paris, France
[f] Ilse Katz Institute for Nanoscale Science and Technology, Department of Materials Engineering, Ben-Gurion University of the Negev, Beer-Sheva, 8410501, Israel
[g] The Polytechnic School (TPS), & The School of Engineering of Matter, Transport and Energy (SEMTE), Ira A. Fulton Schools of Engineering, Arizona State University, Mesa, AZ, 85212, USA. E-mail: Kenan.song@asu.edu

† Electronic supplementary information (ESI) available. See DOI: https://doi.org/10.1039/d2tc01109c

This journal is © The Royal Society of Chemistry 2022

Published on 14 suoidnemánnu 2022. Downloaded on 2026-06-02 13:51:14.

units would restrict their maneuverability and the distance they can travel safely, especially in complex unstructured spaces and extreme conditions, such as the human in-body system for targeted drug delivery or deep-sea wet-environment.[4] On the other hand, smart materials or systems, such as shape memory polymers (SMPs), exhibit multimodal shape manipulation with exposure to external stimuli (*e.g.*, pH, stress, light, thermal, electric, or magnetic field).[5,6] With proper manipulation of the external fields and appropriate materials (*i.e.*, SMPs containing nanoparticles for advanced hybrids or composites), SMPs can function efficiently with reversible shape transformation or precise motions.[7]

Even though many external stimuli can control shape memory effects, not all are favorable for providing both hovering and translational motions essential for an active robot. For example, the commonly used heat and light stimulation can perform an actuation in a fixed position and change the footprint (*e.g.*, area and volume), but will find it challenging to constantly move the object in space (*e.g.*, dark outer space).[8] In contrast, magnetic field-induced stimulation can hover the object at a single point with tailored magnetic field strength or move the object using magnetic forces to multiple locations.[9] However, applying a magnetic field to materials with homogeneous compositions is usually insufficient for changing the product shape, dimensions, or morphologies. Therefore, it is urgent to develop a multi-material system with dual or more actuation mechanisms. For example, fixing complex shapes of a manufactured object without the presence of the external field is problematic in SMPs since most of them are elastomers considered to display a rubbery nature with a low Young's modulus.[2] As a result, developing new manufacturing mechanisms to include more chemical components or extra physical microstructures in composite systems can potentially offer dual or multiple stimuli-responsiveness, which is desirable for unique applications (*e.g.*, shape fixability and movement flexibility).

Conventionally, researchers have adopted simple molding or casting processing to fabricated stimuli-responsive soft actuators using multiple materials. For example, Liu *et al.* used polydimethylsiloxane (PDMS) and graphene oxide to fabricate stimuli-actuated soft robots.[10,11] Recently, many research groups have adopted 3D printing as a powerful tool to fabricate highly customized, complex-shaped soft actuators for various applications. For instance, Zhao *et al.* developed a magnetic field-assisted, ink-based 3D printing process to fabricate small-size, magnetic field-responsive robots with complex shapes (*e.g.*, kirigami structures).[12] Qi *et al.* used direct ink writing (DIW)-based 3D printing for fabricating thermo- and photo-responsive composites using a few bio-inks.[13,14] These approaches relied upon a single nozzle to deposit specific types of materials and structures with usually singular stimuli-responsiveness. To overcome this, Lewis *et al.* reported a new multi-material, multinozzle 3D printing (MM3D) that fabricated voxelated soft matters (*e.g.*, silicone, wax, petroleum jelly, epoxy silica, gelatin) and provided dual or multi-stimuli-responsiveness.[15] However, the domain size of individual material addition is limited to the nozzle diameter and rheology *via* this approach. Though a higher number of printheads can enrich chemical compositions or physical voxels within a printed line, this will enlarge the footprint of a printing platform and induce challenges in machine calibration and multimaterial deposition.

To efficiently use the advantages of the above-mentioned approaches and overcome a few of the obstacles, we use multiphase direct ink writing (MDIW) as a 3D printing technique to print in-plane (*i.e.*, *x*/*y*-axis) multiphase and out-of-plane (*i.e.*, *z*-axis) multilayers for fabricating stimuli-responsive structures that can be activated by heat and magnetic fields. The MDIW can extrude two feedstocks *via* inlets of our specially designed nozzle (*i.e.*, printhead) in the form of polymer gels and rearrange them in the layer multipliers forming alternating layers within individually printed lines.[16] The MDIW, unlike any other 3D printer, can assemble materials at specific locations that would provide necessary multimodal movement for flexibly designed and fabricated SMP structure. The two 3D printing feedstocks include (i) a soft ester-based thermoplastic polyurethane (TPU) mixed with iron oxide (Fe_3O_4) nanoparticles, providing magnetic field response, and (ii) a stronger ether-based TPU mixed with polycaprolactone (PCL), offering heat responsiveness. By accurately controlling the rheology of the feedstocks, each printed line consists of 64 alternating layers in the *xy*-plane (*i.e.*, precision at μm) and three, five, and ten out-of-plane layers (*i.e.*, 3L, 5L, 10L) along the *z*-axis. In addition, the fabricated samples were tested for their mechanical and thermal properties to predict the transition temperatures for further manipulating their actuation responsiveness to thermal and magnetic fields.

Experimental

Materials

Ellastollan TPU-B (ETPU-B) and ellastollan TPU-D (ETPU-D) were provided by BASF, USA. ETPU-B is a polyester-based TPU with an A-scale Shore hardness, with a density of 1.18 g cm^3, a tensile strength of 25 MPa, and ~900% elongation at a break. ETPU-D is a polyether-based TPU with a D-scale Shore hardness, with a density of 1.17 g cm^3, a tensile strength of 60 Mpa, and ~470% elongation at a break. Comparatively, ETPU-B has higher ductility and lower stiffness/strength than the ETPU-D, with the former elastomer functioning for shape memory and the latter for shape fixation. PCL (CAS-No. 24980-41-4) with a molecular number of 80 000 in the form of pellets was purchased from Millipore Sigma, USA. The PCL is a biodegradable polyester with a low melting point of 60 °C to stimulate the actuation. Synthetic black iron oxide (Fe_3O_4 > 98%) nanoparticles with an average particle size of 300 nm in diameter were purchased from Alpha Chemicals, USA. Phenylbis (2,4,6-trimethyl benzoyl) phosphine oxide (Irgacure 819 (IR819), 97% assay, CAS-No. 162881-26-7) and dimethylformamide (DMF) (anhydrous ≥ 99.8%, CAS-No. 68-12-2) were from Millipore Sigma, USA. All the materials were used as received without any modification.

Published on 14 suoidnemánnu 2022. Downloaded on 2026-06-02 13:51:14.

3D printing feedstock formulation

Our unique additive manufacturing platform (Fig. 1 with the in-house developed printhead in Fig. S1, ESI†) will demonstrate the use of two feedstocks (*i.e.*, ETPU-B/Fe_3O_4 and ETPU-D/PCL in Fig. 1a), though more raw materials can be used for multi-material 3D printing. The first feedstock consists of ETPU-B dissolved in DMF and Fe_3O_4 dispersed in the prepared ETPU-B/DMF solution (Fig. 1a). Varying nanoparticle concentrations in the polymer-nanoparticle combinations (Fig. 1a) were tested to achieve the required rheological characteristics (Fig. S2 and S3, ESI†). Specifically, the polymer was dissolved under a constant mechanical stirring at 110 °C for 3 h while the beaker was covered using a parafilm to keep the solution clean and prevent solvent evaporations. Once the ETPU-B was completely dissolved, the hotplate was turned off, then proper concentration of Fe_3O_4 particles were added and dispersed *via* high-speed mechanical stirring for 30 min. The second feedstock consists of ETPU-D and PCL dissolved in DMF. Various ETPU-D concentrations and ETPU-D/PCL combinations were tested during the processing to achieve similar rheological properties to the first feedstock (ETPU-B/Fe_3O_4/DMF) (Fig. S2, ESI†). Specifically, the PCL pellets were added after ETPU-D dissolved into DMF under constant mechanical stirring at 110 °C for 3 h and protected using a parafilm from contamination and solvent evaporations. The solutions were mixed with IR819 to improve light absorption for UV curing and degassed for removing any air bubbles using bath sonication for 1 h before use. Table S1 (ESI†) summarizes the material and feedstock formulation nomenclature for both the feedstocks.

Characterization

The rheology studies were conducted for both the feedstocks using a cone-and-plate setup at room temperature (Discover Hybrid Rheometer 2, TA Instruments). The samples were dropped on a 40 mm, 2° Peltier steel cone plate using a pipette. The viscosity and shear thinning properties were done at an increasing strain rate of 0.001–8000 s^{-1}, with a truncation gap of 100 μm and a trim gap of 50 μm. Any overflow of the sample was cleaned to the plate edge before performing the test to prevent edge fracture for accurate results. Amplitude sweep was conducted with the same geometry at 1 Hz frequency and a logarithmic strain sweep from 0.1–10 000%. Similarly, a frequency sweep was conducted with the same geometry from 0.1–600 rad s^{-1} at a 10 s^{-1} shear rate. A step-strain rheological analysis was conducted at 1 Hz frequency with a varying strain of 0.01 to 1 in every alternate cycle. The tensile tests were conducted at room temperature using a dynamic mechanical analyzer (DMA) (Discover Hybrid Rheometer 2, TA Instruments). All the samples were air-dried and solvent-free before testing with a constant gauge length of 10 mm and sample size of 5 mm in width and 0.02 mm in thickness (Fig. S4, ESI†). The thermal properties of the raw materials and the 3D printed multiphase composites were measured using a differential scanning calorimetry (DSC) (Discovery DSC 250, TA Instruments) at a ramp rate of 10 °C min^{-1} from −80 °C to 250 °C in a nitrogen atmosphere to detect the actuation temperature (Fig. S5, ESI†).

A physical property measurement system (PPMS) with a vibrating sample magnetometer (VSM) attachment was used for measuring the change in the magnetic moment with respect to the magnetic field at room temperature from −1 T to 1 T at a ramp rate of 25 mT (model 6000, Quantum Design, USA). The measurement was done both parallelly and perpendicularly to the layers in the *xy*-axis before conducting experimental studies using an electromagnetic coil system. A customized electromagnetic coil system consisting of eight electromagnetic coils

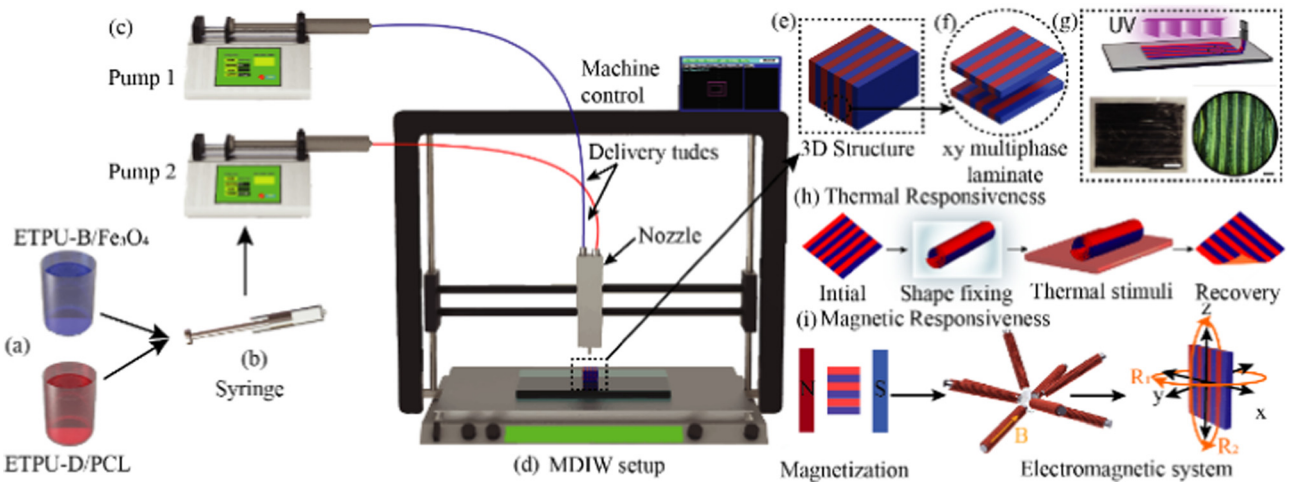

Fig. 1 The Multiphase Direct Ink Writing (MDIW) 3D printing system demonstrating (a) two feedstocks of ETPU-B/Fe_3O_4 and ETPU-D/PCL to feed the (b) stainless steel syringes (*i.e.*, one for each solution), (c) two separate syringe pumps connected to the two inlets of the printhead nozzle, (d) MDIW 3D printing platform consisting of the machine control, delivery tubes connect to the syringe, and the multiphase nozzle as the 3D printhead, (e) MDIW-printed multiphase 3D structures consisting of (f) stacking of the laminate thin-ply along the *z*-axis and layers within the *x*/*y*-plane, (g) UV curing of a printed laminate using a 60 W, 405 nm UV led lights with a digital photograph of the as printed large-area laminate (scale bar: 10 mm), and a zoomed-in optical image showing the layer formation (scale bar: 100 μm), an illustration of step-by-step (h) thermal actuation procedures, and (g) magnetic actuation procedures using an electromagnetic system.

 This journal is © The Royal Society of Chemistry 2022

Published on 14 suoidnemánnu 2022. Downloaded on 2026-06-02 13:51:14.

was used for performing the magnetic actuation tests and demonstrations. The magnetic field direction and gradient were controlled by the input received from the user *via* an Xbox PC controller and python for recording the experimental data. The system is also equipped with three Logitech C920 high-speed cameras to capture the top, side, and front views of different sample movements in the 3D space.

Results and discussion

Layered structures with property variations or dimensional transitions in different layers have been reported to have intelligent behaviors, such as stimuli-responsiveness as a function of external environmental conditions.[17,18] For example, different locations in laminate layers respond to the same temperature based on their thermal expansion coefficients. However, conventional manufacturing of layered composites has been primarily limited to the manual placement of polymers and fibers/fabrics (*e.g.*, lack of efficiency in stacking epoxy/carbon fiber fabric layers).[19] Therefore, we would demonstrate our in-house 3D printing for rapidly prototyping layers along the *z*-axis and simultaneously generating sublayers within the *x*/*y* in-plane directions. Fig. 1 illustrates the MDIW 3D printing platform for processing multiphase, multi-layered composite samples and the anisotropic layer-structure enabled thermal and magnetic actuation. Since the MDIW layering mechanism has been explained in our previous publication,[16] we will primarily discuss the newly updated layer multiplying & polymer nanoparticle assembly processes not reported before.

To demonstrate the stimuli-responsiveness in layers, each layer must contain different compositions or structures that need to be assembled *via* our unique multi-material printing.[20] For example, once the feedstocks were prepared (*i.e.*, ETPU-B/Fe_3O_4 and ETPU-D/PCL, Fig. 1a), they were loaded into two separate syringes and syringes pumps (Fig. 1b and c). The syringes were connected to the two inlets of the print head using nylon tubes. The solutions were pumped at a constant flow rate of 1 mL min^{-1} to transport printing feedstocks to the printhead (*i.e.*, nozzle in Fig. 1a). The MDIW 3D printing platform (Fig. 1d) is equipped with the machine control unit to control printhead position and travel and the 60 W, 395–405 nm UV LED lights for immediate post-curing of deposited feedstocks. The MDIW nozzle is uniquely designed and 3D-printed using a metal 3D printer with Inconel 718 metals. The nozzle consists of four parts (I) spinneret, (II) minimizer, (III) layer multiplier, and (IV) reducer (Fig. S1 and Movie M1, M2, ESI†). The layer multiplication happens in the layer multiplier units where the incoming flow is divided into two parts horizontally and rearranged vertically, duplicating each feedstock series (*e.g.*, ETPU-B/Fe_3O_4-ETPU-D/PCL) and replacing one beside the other within the *x*/*y* in-plane directions (Fig. S1, ESI†). As a result, the number of *n* layer multipliers will form $2^{(n+1)}$ alternating sublayers of the feedstocks. Moreover, each printing layer's immediate post-curing and solidification helped generate distinct layers within the 3D structure with limited inter-layer diffusion or layer disruptions (Fig. 1e and f). To have simple demonstrations, we only printed three different sample thicknesses consisting of 3L (180 μm), 5L (300 μm), and 10L (710 μm) along the *z*-axis direction, while the *x*/*y* in-plane directions had 64 alternating layers within each printing line (*e.g.*, in-plane layer domain size ~100 μm). Fig. 1g illustrates the UV curing process of the printed laminate layers with a photograph of the printed laminate texture and a zoomed-in optical image clearly showing the layer formation (*i.e.*, black regions of ETPU-B/Fe_3O_4/DMF and transparent white regions of ETPU-D/PCL/DMF). Fig. 1h and i illustrate the thermal and magnetic actuation mechanism enabled by the layered structures readily achieved in our unique MDIW 3D printing method.

The uniform and continuous layer formability were possible only due to the precise rheological behavior control in both feedstocks (*i.e.*, the ETPU-B/Fe_3O_4/DMF *vs.* ETPU-D/PCL/DMF suspensions). The rheology was conducted on samples containing various polymer and nanoparticle concentrations. As a result, there is a matching of viscosity between samples of (i) 62.25 wt% ETPU-B/7.5 wt% Fe3O4 and (ii) 15 wt% ETPU-D/20 wt% PCL (Fig. S2, ESI†). Also, the shear-thinning behavior of both feedstocks facilitated the 3D printing without clogging that disrupts layer formations. Additionally, amplitude sweeping, frequency sweeping, and step-strain cyclic analyses were conducted on both feedstocks to understand the rheological stability (Fig. S3, ESI†). The higher loss modulus values than the storage moduli indicated the more liquid features of printing feedstocks (Fig. S3a and b, ESI†), facilitating the printing continuity. The slightly lower storage modulus of ETPU-B/Fe_3O_4 than ETPU-D/PCL was probably due to the nanoparticle effect. More importantly, the cyclic step-strain analysis confirmed the stability of both printing feedstocks as alternating layers at lower and higher shear rates (Fig. S3c and d, ESI†)."

The combination between mechanical stiffness and ductility is critical in forming thermal responsiveness, such as the shape-memory effect.[21] For example, the ETPU-B has a strength of 25 MPa and ductility of >900%, while the ETPU-D has a strength of 60 Mpa and strain ~450%. The mechanical properties of the composites were tested using the 3L multiphase samples as an example, and other layered samples showed similar behaviors since the only change is in the sample thickness and layer quality consistency. When loaded with different polymers and nanoparticles for the layered texture printing, the composites (Fig. 1e and f) showed anisotropic mechanical properties (*i.e.*, 126 ± 15 MPa and 85 ± 6 MPa for modulus along the *x*-axis and *y*-axis direction, respectively, see stress–strain curves in Fig. S4 and Table S2, ESI†). More importantly, the higher modulus in ETPU-D/PCL (*i.e.*, modulus averaged ~1084 MPa) would benefit the shape fixation, and comparatively, the lower modulus in ETPU-B/Fe_3O_4 (*i.e.*, modulus averaged ~61 MPa) would facilitate the shape recovery. Besides, the sample had high ductility along the *x*-axis with a strain >330% when no fracture was observed even at the maximum limit of the tensile tester (Table S2, ESI†). However, the sample fractured at a strain of 115 ± 12% along the *y*-axis (Table S2, ESI†). It is noteworthy mentioning that the shape

Published on 14 suoidnemánnu 2022. Downloaded on 2026-06-02 13:51:14.

morphing strains during our actuation demonstration would be much smaller than the strain limit within the elastic regime (Fig. S4, ESI†) due to different layer tensions/compressions, ensuring unlimited cycles of shape recovery and mechanical durability for broad applications. The fracture strength along the *y*-axis was ~23 ± 2.5 MPa and the toughness was ~21 ± 3.6 MPa. The fracture strength and toughness were not obtained along the *x*-axis since the samples did not fracture till the maximum limit of the machine.

To achieve the thermal actuation function, it is required to obtain the transition temperature to initiate the shape recovery process. Therefore, the DSC analysis was done on all three thicknesses (*i.e.*, 3L, 5L, and 10L composite layers), the native composites (ETPU-B/Fe_3O_4 and ETPU-D/PCL), and the raw polymers (*i.e.*, ETPU-D, ETPU-B, and PCL) used for making the feedstocks (Fig. S5, ESI†). The TPUs used in the feedstocks either had a low glass transition (T_g) or a very high melting temperature (T_m), which was consistent with the TPU properties that ensured the thermal stability (*e.g.*, TPU T_m ~175 °C, much higher than the PCL T_m ~60 °C, Fig. S5, ESI†). Also, note that the ETPU-B/Fe_3O_4-ETPU-D/PCL composite layers showed a lower T_m of ~50 °C than the pure PCL (*i.e.*, with a T_m of ~60 °C) due to the mixture of amorphous TPU in semicrystalline PCL. The native feedstocks also show consistent trends as the raw polymers due to less complexity in the composite polymer chain entanglement and interaction (Fig. S5a *vs.* b *vs.* c, ESI†). The multiphase composite contained two kinds of TPUs, and the PCL showed consistent thermal properties in composites, for example, with the PCL onset melting point at ~40 °C, peak melting point at ~50 °C, and ending at ~60 °C with the layer number changing from three to five and ten. Based on this DSC analysis, thermal actuation studies were thus conducted at ~40–60 °C to show the actuation efficiency, showing varying responsiveness starting from the shape fixing at room temperature (25 °C).

Thin-layer rolls have advantages of low footprint, higher impact resistance, and small thermal expansions, with broad applications in aerospace and space missions.[22] Therefore, 3 × 3 cm square-sized samples were cut from 5L composite layers and displayed the actuation following procedures from fixed rolling to full expansion stages, as depicted in Fig. 1h. Specifically, the samples were rolled *via* the DMA in the furnace-controlled oven (FCO) and frozen at −20 °C for 20 min to fix the shape, with a fixation efficiency of ~90%. Placing different samples on a hotplate with the temperature control initiated the unrolling with different rates, generating the sample structure-temperature-responsiveness relationships and reflecting the actuation efficiency (Fig. 1h). Each actuation was done three times at each temperature for statistical consistency.

Fig. 2 shows the responsiveness variations for the composite samples with varying rolling directions (*i.e.*, rolled along with the layers in Fig. 2a, perpendicular to the layers in Fig. 2b, and diagonally in Fig. 2c). The sample did not recover at room temperature (25 °C) until 6 min, irrespective of the rolled direction (retained rolled structures in inserted photos of Fig. 2a–c), showing consistent shape fixing efficiency. Comparatively, at a temperature of 40 °C, the perpendicular rolled sample showed a full-expansion time of ~120 s (Fig. 2b), 30 seconds faster than that rolled along with the layers (Fig. 2a) and 20 s faster than the diagonally-rolled sample (Fig. 2c). Similarly, other temperature fields exhibited different durations of actuation when rolled along with different directions concerning the printing textures. For example, at the actuation of 50 °C, the perpendicular-to-layer rolling showed the actuation of ~65 s (Fig. 2b), while the parallel-to-layer rolling direction showed the unrolling time of ~75 s (Fig. 2a) and 45°-rolling of a 70 s (Fig. 2c). The increase in actuation temperature reduced the responsiveness differences among different samples. Consistently, these differences in the recovery time were 10 s and 5 s from perpendicularly-rolled (Fig. 2b) to parallelly-rolled (Fig. 2a) and diagonally-rolled (Fig. 2c) samples, respectively, at the temperature of 50 °C; these differences further decreased to be within 1–2 s at an actuation temperature of 60 °C among different samples. Movie S3–S5 (ESI†) shows the recovery process of the parallel-rolled, perpendicularly rolled, and diagonally rolled samples, respectively, at a temperature of 60 °C as examples. The faster recovery with increasing temperatures was correspondingly controlled by the PCL's melting and polymer chain reorganization behavior, which was identified by the DSC analysis. The thermal conduction of the samples also helped tune the actuation time

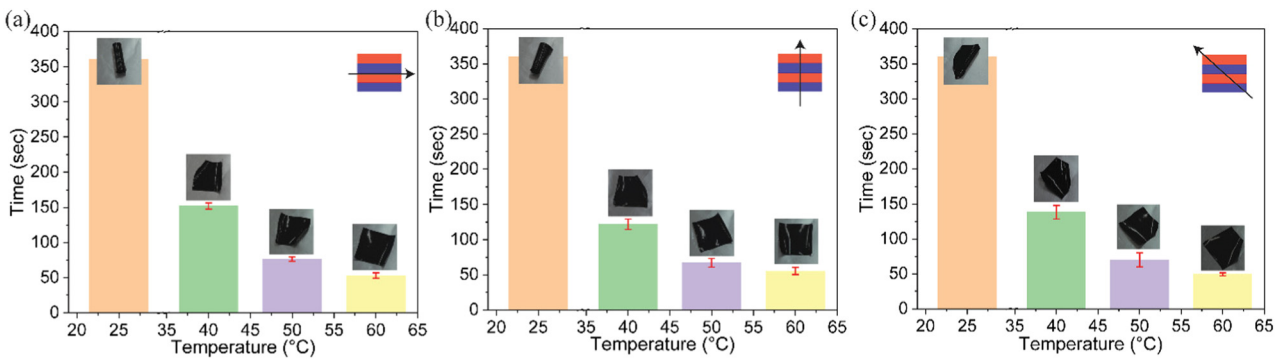

Fig. 2 Thermal-responsiveness demonstration study showed the response time as a function of temperature for 5L multiphase samples rolled (a) along with the layers (arrow direction in the insert figure), (b) perpendicular to the layers (arrow direction in the insert figure), and (c) diagonally at 45° (arrow direction in the insert figure) with photographs showing the corresponding morphing stages.

 This journal is © The Royal Society of Chemistry 2022

Published on 14 suoidnemánnu 2022. Downloaded on 2026-06-02 13:51:14.

with increasing temperatures. Fig. S6 (ESI†) shows thermal imaging of the post-actuation samples suggesting good thermal conductivity to facilitate the thermal actuation. Irrespective of the rolled direction, the to-be-stimulated samples were compliant to the hotplate-programmed temperatures and started cooling down upon exiting the heat environment. More quantitative studies of the thermal actuation efficiency and rates will be done to understand the time-temperature-dimension relationship of the shape-memory effects in our future work.

The fabricated multiphase composite samples consist of the Fe_3O_4 magnetic nanoparticles that were selectively positioned and preferentially patterned along with the polymeric chains due to the flow shear experienced by the feedstock solutions.[23,24] Magnetometric measurements were done on the 3L sample by generating an MH curve to determine the magnetic property with changing magnetic strength and its anisotropy (Fig. 3).[25] Higher magnetization was obtained in the layer-parallel direction (*i.e.*, along-layers) than in the perpendicular direction. In addition, the patterning of the Fe_3O_4 particles with the polymer chain in a defined space causes a directional dependence allowing for an anisotropic response to magnetism in a 3D space (*i.e.*, *x*/*y*/*z*-axis).

The magnetic actuation studies were conducted in a custom electromagnetic coil system made of eight coils. Samples of the required shape were cut precisely and pre-magnetized before performing the experimental tests (Fig. 1i) by placing them in between the opposite poles of neodymium (NdFeB) N52 permanent magnets. The magnetized sample was put inside a cubical glass container of size 5 × 5 × 5 cm filled with 50% glycerine, 25% distilled water, and 25% methanol to give untethered motion and actuation control over composite layers by reducing wall and air friction. The system can enable five degrees of freedom (DOF) with the rotation about the magnet's main axis not achievable.

The electrical current required to obtain the desired force (F) and torque (T) on the magnetized sample with a magnetic moment (M) can be determined by,[26,27]

$$F = \begin{bmatrix} \frac{\partial B}{\partial x} & \frac{\partial B}{\partial y} & \frac{\partial B}{\partial z} \end{bmatrix}^T M \quad (1)$$

$$T = M \times B \quad (2)$$

$$\begin{bmatrix} i_0 \\ . \\ . \\ . \\ i_n \end{bmatrix} = \begin{bmatrix} \beta(P) \\ M^T \beta_x(P) \\ M^T \beta_y(P) \\ M^T \beta_z(P) \end{bmatrix} \begin{bmatrix} B_{\text{desired}} \\ F_{\text{desired}} \end{bmatrix} \quad (3)$$

where β is the magnetic field contribution from each of the eight coils at a position P. β_x, β_y, and β_z are the calibration gradient matrix in the *xyz*-axis, respectively. B_{desired} and F_{desired} are the flux density and force, respectively, in each direction. eqn (1) can be simplified using a pseudoinverse as,

$$I = A_{B,F}(M, P)^{\dagger} \begin{bmatrix} B_{\text{desired}} \\ F_{\text{desired}} \end{bmatrix} \quad (4)$$

The magnetic field, H, can also be calculated as per,

$$H = B/\mu_0 \quad (5)$$

where μ_0 is the vacuum permeability constant given as $4\pi \times 10^{-7}$ Tm A^{-1}.[28]

Inside the electromagnetic coil system, these multiphase samples made of ETPU-B/Fe_3O_4 and ETPU-D/PCL can be considered to be a wireless robot due to their untethered controlled translational, and rotational motion. Due to the frictionless motion, the magnetized samples always prefer to be aligned with the direction of the magnetic field. Therefore, by changing the direction of B, the robot's orientation can be changed, and while applying F, the robot moves in the direction of the applied force (*e.g.*, steering forward or propelled). The electromagnetic system is enabled with a python program to record the results for orientational and positional analyses.

The 10L samples, which have comparatively higher rigidity and magnetic strength than the 3L and 5L composites, were used for the magnetism-actuation demonstration. Two samples in an arrowhead shape, with one having the layers in the same direction (parallel) as the arrowhead (sample-R_a) while the other having layers perpendicular to the arrowhead direction (sample-R_p), were cut and magnetized in the direction of the layers (inserts in the first column top right corner Fig. 4a and b). The samples were magnetized along the layer direction because of the larger magnetic strength parallel to the layers than in the perpendicular direction, as seen from the VSM analysis (Fig. 3). Fig. 4 shows the snapshots for the response of the samples with respect to changing flux. The red, green, and blue lines are the direction of the applied B in the *xyz*-axis, respectively, and the inserts in the bottom right corner are the movement of the sample on the *z*-axis. In the case of sample-R_a, the arrowhead aligned in the same direction as B (Fig. 4a),

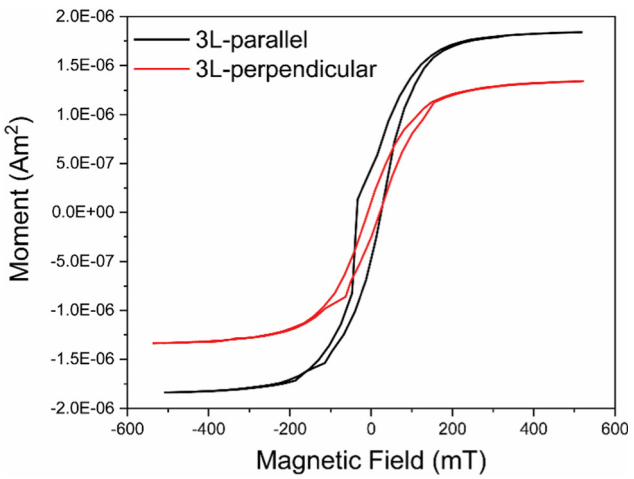

Fig. 3 MH curve at room temperature measured parallel and perpendicular to the *x*/*y* layer of the 3L samples.

Published on 14 suoidnemánnu 2022. Downloaded on 2026-06-02 13:51:14.

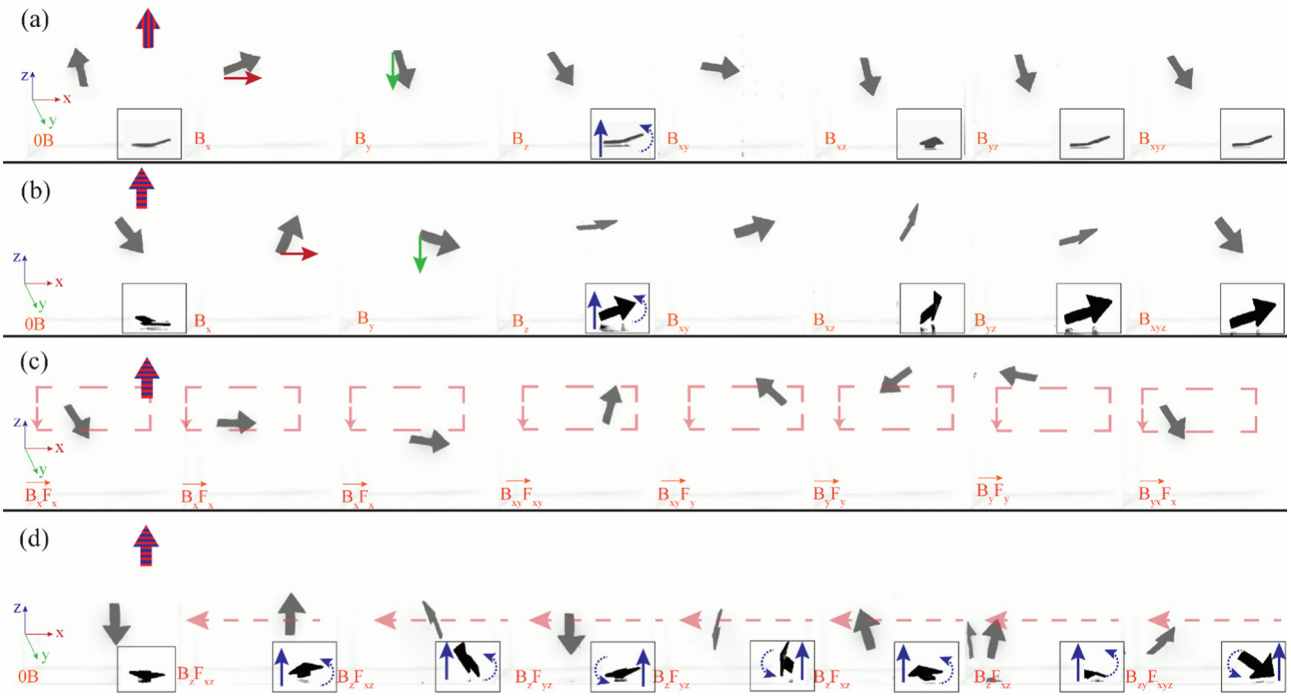

Fig. 4 Magnetic actuation study using an arrow-shaped sample with layers (a) in the same direction as the arrowhead and (b) perpendicular to the arrowhead. (a and b) shows the response of the arrowhead (top view of the arrow at the center) with respect to the applied magnetic field (*B*) direction represented with the red, green, and blue arrows for the *x*, *y*, and *z*-axis, respectively. The inserts at the bottom right corner represent the side view of the arrowhead. (c) represents a translation movement of the arrowhead with respect to the applied magnetic field (*B*) and force (*F*) in the *xy*-axis. The electromagnetic system was programmed to move the arrow along a pre-defined path represented by the pink arrow. (d) represents a combination of flipping and linear movement of the arrowhead with respect to the magnetic field (*B*) and force (*F*) direction in the *xyz*-axis directions. The pink arrow represents the linear *xy* movement, and the blue arrows represent the flipping movement rotating the *y*-axis within the *xz*-plane.

i.e., when *B* was on the *x*-axis (B_x), the arrowhead turned to the flux direction. It was challenging to align the sample on the *z*-axis due to a greater downward pull (gravity) than the magnetic strength caused due to the dimension and weight of the sample. However, as seen from the *z*-axis inserts, the sample tried to move in the direction of B_z to stand straight. Similar observations were made for sample-R_p, *i.e.*, the arrowhead aligned with respect to *B*, which depends on the magnetization direction parallel to the layers. Therefore, the arrowhead moved perpendicular to the applied flux (Fig. 4b). It was relatively easier to move the sample to the *z*-axis because of the difference in the layer direction and dimension of the sample showing the anisotropic behavior. Due to the better responsiveness of sample-R_p, further studies were done using only this sample.

Fig. 4c and d show demonstrations using the sample-R_p, where in addition to a magnetic field (*B*), a directional force (*F*) was applied to give a translation motion to the sample. The arrowhead, which resembles a fish head-tail-like shape, was made for swimming in a fixed path marked with pink lines in Fig. 4c (Movie S6, ESI†). A linear motion was not possible due to the hard-to-eliminated surface friction, and hence the sample had to be wiggled in the *xy*-axis continuously (swim) to give a forward motion. Similarly, the sample was made to flip and move from right to left, shown with a pink line in Fig. 4d, to demonstrate the motions in all three axes together (Movie S7, ESI†). Due to the layer and magnetization direction, the arrowhead was able to flip only when aligned in the *x*-axis direction. Hence after every flip, the sample was rotated around the *y*-axis. This example demonstrated the controlled maneuverability within a tiny space using a simple magnetic field. Due to the electromagnetic coil system requirements for safe use, the dimension of magnetized samples was limited, which also affected the responsiveness. Movie S8 (ESI†) shows an example of the high degree of responsiveness obtained with a relatively smaller sample clearly showing the untethered microrobot movability. With a higher magnetic field, the Fe_3O_4 particles can enable an inductive heating effect, which can cause simultaneous control of thermal and magnetic actuation that we will study in our future work.[29,30] Table S3 (ESI†) gives more examples of magnetic actuation of SMPs with different materials, nanoparticles, and fabrication systems. These magnetic and thermal stimuli-responsive SMPs using 3D printing can be customized to specific applications, especially in the medical field for drug delivery *via* untethered navigation inside an animal or human body or biosensing for magnetic resonance imaging (MRI).[31–33] More combinations of polymers and nanoparticles have also been studies for stimuli responsive actuations for various other applications as summarized in Table S4 (ESI†).

Conclusion

We have successfully demonstrated the one-step fabrication of a dual-stimuli responsive SMP using an in-house developed

 This journal is © The Royal Society of Chemistry 2022

Published on 14 suoidnemánnu 2022. Downloaded on 2026-06-02 13:51:14.

MDIW 3D printing mechanism for composite multilayers controlled by the magnetic field and thermal stimuli. The perfect rheology control assisted in printing lines consisting of 64 alternating in-plane layers (*i.e.*, an individual sublayer domain size of ~100 μm), producing a high degree of nanoparticle and polymer chain assembly. The thermal actuation was programmed based on the DSC transition temperature analysis that allowed a wide temperature operating window (*i.e.*, 40–60 °C), showing different recovery rates depending on external thermal conditions and rolled directions. Even with a minimal 7.5 wt% concentration of the Fe_3O_4 nanoparticles, the alignment of these nanoparticles within the polymer matrix produced high magnetic strength and enabled wireless control of the SMP in an electromagnetic coil system. These programable actuators with precise directional control suggest broad applications in structural support, thermal exchange, anisotropic conductors, optical surface patterning, biomedical scaffolds as targeted drug delivery, MRI diagnosis, field/space exploration devices, flexible robotics, wearable electronics, and many more.

Author contributions

D. R. – conceptualization, data curation, formal analysis, investigation, methodology, validation, visualization, writing – original draft, review & editing. R. B./R. J./M, I./H. M. – methodology, resource, software. G. M./Y. G. – resources, writing – review & editing. KS – conceptualization, funding acquisition, methodology, project administration, resource, supervision, writing – original draft, review & editing.

Conflicts of interest

There are no conflicts of interest to declare.

Acknowledgements

We acknowledge the support from the United States – Israel Binational Science Foundation (BSF) (award #2020/102) and FACE Foundation (award #AWD00035441). Thanks are given to professor Sefaating Tongay at ASU for his consultation on magnetic property measurements and for providing us with the necessary resources and BASF for providing raw materials.

References

1 W. Hu, G. Z. Lum, M. Mastrangeli and M. Sitti, *Nature*, 2018, **554**, 81–85.
2 Q. Ze, X. Kuang, S. Wu, J. Wong, S. M. Montgomery, R. Zhang, J. M. Kovitz, F. Yang, H. J. Qi and R. Zhao, *Adv. Mater.*, 2020, **32**, 1–8.
3 J. Kim, S. E. Chung, S. E. Choi, H. Lee, J. Kim and S. Kwon, *Nat. Mater.*, 2011, **10**, 747–752.
4 C. Majidi, *Adv. Mater. Technol.*, 2019, **4**, 1822477.
5 W. Xu, S. Jambhulkar, Y. Zhu, D. Ravichandran, M. Kakarla, B. Vernon, D. G. Lott, J. L. Cornella, O. Shefi, G. Miquelard-Garnier, Y. Yang and K. Song, *Composites, Part B*, 2021, **223**, 109102.
6 W. Xu, Y. Zhu, D. Ravichandran, S. Jambhulkar, M. Kakarla, M. Bawareth, S. Lanke and K. Song, *ACS Appl. Nano Mater.*, 2021, **4**, 7538–7562.
7 C. Xin, D. Jin, Y. Hu, L. Yang, R. Li, L. Wang, Z. Ren, D. Wang, S. Ji, K. Hu, D. Pan, H. Wu, W. Zhu, Z. Shen, Y. Wang, J. Li, L. Zhang, D. Wu and J. Chu, *ACS Nano*, 2021, **15**, 18048–18059.
8 C. Yuan, Z. Ding, T. J. Wang, M. L. Dunn and H. J. Qi, *Smart Mater. Struct.*, 2017, **26**, 105027.
9 J. E. Park, J. Jeon, J. H. Cho, S. Won, H. J. Jin, K. H. Lee and J. J. Wie, *RSC Adv.*, 2019, **9**, 11272–11280.
10 X. Wang, N. Jiao, S. Tung and L. Liu, *ACS Appl. Mater. Interfaces*, 2019, **11**, 30290–30299.
11 X. Hu, Z. Ge, X. Wang, N. Jiao, S. Tung and L. Liu, *Composites, Part B*, 2022, **228**, 109451.
12 Y. Kim, H. Yuk, R. Zhao, S. A. Chester and X. Zhao, *Nature*, 2018, **558**, 274–279.
13 X. Kuang, Q. Mu, D. J. Roach and H. Jerry Qi, *Multifunct. Mater.*, 2020, **3**, 045001.
14 J. Wu, Z. Zhao, X. Kuang, C. M. Hamel, D. Fang and H. J. Qi, *Multifunct. Mater.*, 2018, **1**, 015002.
15 M. A. Skylar-Scott, J. Mueller, C. W. Visser and J. A. Lewis, *Nature*, 2019, **575**, 330–335.
16 D. Ravichandran, W. Xu, M. Kakarla, S. Jambulkar, Y. Zhu and K. Song, *Addit. Manuf.*, 2021, **47**, 102322.
17 Q. Zhang, J. Wommer, C. O'Rourke, J. Teitelman, Y. Tang, J. Robison, G. Lin and J. Yin, *Extreme Mech. Lett.*, 2017, **11**, 111–120.
18 H. Du, L. Liu, F. Zhang, J. Leng and Y. Liu, *Composites, Part B*, 2019, **173**, 106905.
19 L. Ding, J. Zhang, Q. Shu, S. Liu, S. Xuan, X. Gong and D. Zhang, *ACS Appl. Mater. Interfaces*, 2021, **13**, 13724–13734.
20 S. Thakur and J. Hu, *Aspects Polyurethanes*, 2017, 53–71.
21 D. H. Gracias, *Curr. Opin. Chem. Eng.*, 2013, **2**, 112–119.
22 C. M. Lew, R. Cai and Y. Yan, *Acc. Chem. Res.*, 2010, **43**, 210–219.
23 W. Xu, S. Jambhulkar, D. Ravichandran, Y. Zhu, M. Kakarla, Q. Nian, B. Azeredo, X. Chen, K. Jin, B. Vernon, D. G. Lott, J. L. Cornella, O. Shefi, G. Miquelard-Garnier, Y. Yang and K. Song, *Small*, 2021, 2100817.
24 D. Ravichandran, W. Xu, S. Jambhulkar, Y. Zhu, M. Kakarla, M. Bawareth and K. Song, *ACS Appl. Mater. Interfaces*, 2021, **13**, 52274–52294.
25 S. R. Mishra, M. D. Dickey, O. D. Velev and J. B. Tracy, *Nanoscale*, 2016, **8**, 1309–1313.
26 M. Ilami, R. J. Ahmed, A. Petras, B. Beigzadeh and H. Marvi, *Sci. Rep.*, 2020, **10**, 1–11.
27 R. Ahmed, M. Ilami, J. Bant, B. Beigzadeh and H. Marvi, *Soft Robot.*, 2021, **8**, 687–698.
28 M. P. Kummer, J. J. Abbott, B. E. Kratochvil, R. Borer, A. Sengul and B. J. Nelson, *IEEE Trans. Robot.*, 2010, **26**, 1006–1017.
29 R. Mohr, K. Kratz, T. Weigel, M. Lucka-Gabor, M. Moneke and A. Lendlein, *Proc. Natl. Acad. Sci. U. S. A.*, 2006, **103**, 3540–3545.

30 S. Bai, H. Zou, H. Dietsch, Y. C. Simon and C. Weder, *Macromol. Chem. Phys.*, 2014, **215**, 398–404.
31 S. Martel, J. B. Mathieu, O. Felfoul, A. Chanu, E. Aboussouan, S. Tamaz, P. Pouponneau, L. Yahia, G. Beaudoin, G. Soulez and M. Mankiewicz, *Appl. Phys. Lett.*, 2007, **90**, 24–27.
32 G. Hwang, A. J. Paula, E. E. Hunter, Y. Liu, A. Babeer, B. Karabucak, K. Stebe, V. Kumar, E. Steager and H. Koo, *Sci. Robot.*, 2019, **4**, eaaw2388.
33 F. Zhang, L. Wang, Z. Zheng, Y. Liu and J. Leng, *Composites, Part A*, 2019, **125**, 105571.

Published on 14 suoidnemánnu 2022. Downloaded on 2026-06-02 13:51:14.

 This journal is © The Royal Society of Chemistry 2022